

The integral is evaluated to be just 2 by neglecting the term $k_{FT}^{eff}/2k_F$ in the denominator of the integrand. We obtain then

$$A_c = \frac{16\pi\alpha[1 - \epsilon_0/\epsilon_T(0)]}{k_F^2[\epsilon_T(0)\alpha_{\infty}^*k_F]^2} \quad (C9)$$

*Supported in part by National Science Foundation Grant No. GP7703 and Advanced Research Projects Agency (through Northwestern University Materials Research Center).

¹L. Liu and D. Brust, Phys. Rev. Letters 20, 651 (1968); Phys. Rev. 173, 777 (1968).

²D. Sherrington and W. Kohn, Rev. Mod. Phys. 40, 767 (1968); B. I. Halperin and T. M. Rice, *ibid.* 40, 755 (1968).

³S. H. Groves and W. Paul, Phys. Rev. Letters 11, 194 (1963).

⁴C. F. Lavine and A. W. Ewald (unpublished); C. F. Lavine, thesis, Northwestern University (unpublished).

⁵R. E. Lindquist and A. W. Ewald, Phys. Rev. 135, A191 (1964).

⁶P. Nozieres and D. Pines, Nuovo Cimento 9, 470 (1958); Phys. Rev. 109, 762 (1958); H. Ehrenreich and M. H. Cohen, *ibid.* 115, 786 (1959).

⁷E. D. Hinkley and A. W. Ewald, Phys. Rev. 134,

A1261 (1964).

⁸R. J. Wagner and A. W. Ewald, Bull. Am. Phys. Soc. 11, 829 (1966); R. J. Wagner, thesis, Northwestern University, 1967 (unpublished).

⁹R. B. Dingle, Phil. Mag. 46, 831 (1955).

¹⁰O. N. Tufte and A. W. Ewald, Phys. Rev. 122, 1431 (1961).

¹¹L. Liu and D. Brust, Phys. Rev. 157, 627 (1967).

¹²B. L. Booth and A. W. Ewald, Phys. Rev. Letters 18, 491 (1967).

¹³J. E. Robinson and S. Rodriguez, Phys. Rev. 135, A779 (1964); 137, A663 (1965).

¹⁴J. G. Broerman, Phys. Rev. Letters 24, 450 (1970).

¹⁵D. Sherrington and W. Kohn, Phys. Rev. Letters 21, 153 (1968).

¹⁶L. Liu and E. Tosatti, Phys. Rev. Letters 23, 772 (1969).

¹⁷L. I. Schiff, *Quantum Mechanics* (McGraw-Hill, New York, 1960), p. 169.

Brillouin Scattering Study of Propagating Acoustoelectric Domains in n GaAs^{†*}

David L. Spears[‡]

Department of Physics, Purdue University, Lafayette, Indiana 47907

(Received 15 September 1969)

A Brillouin-scattering study of amplified shear waves in propagating acoustoelectric domains in n GaAs is presented. On the basis of small-signal theory, a complete formalism is developed for the amplification of piezoelectrically active waves from the thermal background of lattice vibrations. Our experimental results show that this provides a good description of the acoustic flux when its intensity is less than about 10^{-2} J/cm³. Here, the growth rate, intensity, frequency distribution, angular distribution, and spatial distribution of the amplified shear waves were all found consistent with small-signal theory. In the subsequent stages of growth, when the acoustic waves become very intense, many interesting deviations from small-signal theory were found, resulting from at least two nonlinear effects, parametric frequency conversion, and enhanced electron-phonon coupling. The acoustic spectrum is rapidly extended to low frequencies, with relatively narrow domains being initially produced at these frequencies. The acoustic energy density tends to saturate at about 1 J/cm³.

I. INTRODUCTION

It is well known that injected ultrasonic waves can be amplified in piezoelectric semiconductors by the application of a sufficiently high electric field¹ because of the strong interaction with mobile charge carriers.² When the drift velocity exceeds the sound velocity, energy and momentum are transferred from the carriers to the acoustic

wave.³ Such interaction with internally generated acoustic waves has been used to explain the electrical instabilities observed in many piezoelectric semiconductors (CdS,⁴ GaAs,⁴ CdSe,⁵ ZnO,⁶ Te,⁷ ZnS,⁸ GaSb,⁹ and InSb¹⁰). These instabilities generally show up as either damped or continuous oscillations in the current. The continuous oscillations are characterized by a high-field domain which propagates with the velocity of sound in the

direction of carrier drift,⁹ and the damped oscillations by a stationary domain located either at the downstream contact or at an inhomogeneity in the bulk of the sample. Brillouin scattering provides a direct means of studying the acoustic waves in the propagating domains, and hence the traveling-wave amplification process. Many such investigations¹¹⁻²¹ in CdS and ZnO have been reported. However, these studies were primarily limited to the final stages in growth of the acoustic waves, and have left unanswered questions with regard to the source of the acoustic waves, the mechanism of domain formation, and the applicability of small-signal theory. With these questions in mind the present study in GaAs was undertaken.

There are many advantages in studying GaAs as opposed to a stronger piezoelectric semiconductor such as CdS or ZnO. The high mobility and weak coupling allows one to work at drift velocities many times the sound velocity and thus minimize the effects of inhomogeneities.^{22,23} In GaAs the domains are relatively wide (~1 mm) and hence are easily resolved. Since GaAs is not birefringent, optical-probe data are much easier to analyze.

Some typical observations are presented in Fig. 1. A constant voltage pulse is applied at $t=0$ to a long rectangular GaAs sample oriented along a $\langle 110 \rangle$ crystallographic direction. The current $j(t)$ shows an initial Ohmic response, but after a period of time (the so-called incubation time) it begins to drop to a saturation level, which is independent of the applied voltage. With a sharply focused light beam, one can detect a narrow domain growing up in the middle of the sample. As shown by the time-position plot, this domain signal grows to a steady-state amplitude and propagates down the sample with the velocity of the piezoelectrically active shear wave (3.35 mm/ μ sec).^{23,24} When the do-

TABLE I. Room-temperature electrical properties of GaAs studied. The calculated frequency of maximum acoustoelectric gain is also shown.

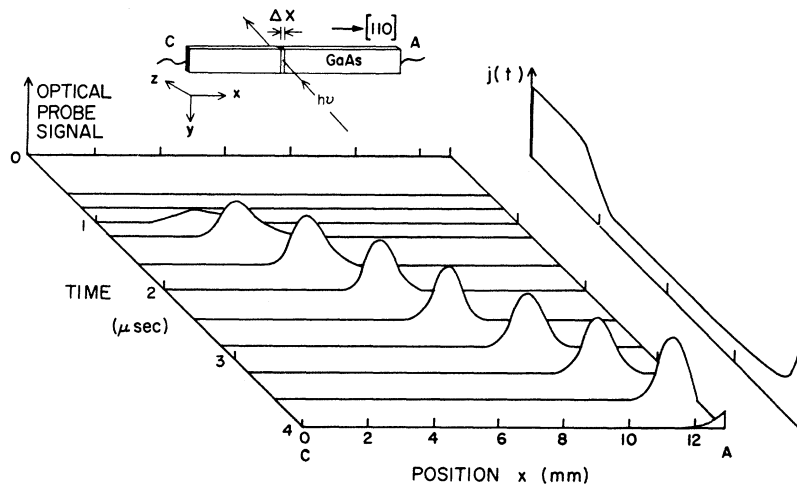
Ingot	n (cm^{-3})	μ ($\text{cm}^2 \text{V}^{-1} \text{sec}^{-1}$)	f_a (GHz)
R	8×10^{14}	7000	4.5
G	4×10^{15}	6000	12
E	5×10^{15}	6000	13
O	6×10^{15}	6000	15

main strikes the anode, it is effectively destroyed and the current rises back to the Ohmic value. The process then repeats itself. These domains can be optically detected in GaAs by either absorption modulation,²⁵ Brillouin scattering, or the birefringence induced by the high electric field in the domain. The latter two techniques are used in the present study.

These measurements were carried out at room temperature on bulk single-crystal n -type GaAs. The carrier concentration (n) and mobility (μ) of the four ingots used are listed in Table I, along with the theoretical frequency f_a of maximum acoustoelectric gain (see Sec. II). Since most samples greater than 1 cm in length exhibited local variations in resistivity of at least 20%, detailed probe measurements²³ on the individual sample were necessary for quantitative analysis.

An incubation time calculated from an estimated thermal-background source intensity has been shown to be consistent with experiment.²⁶ However, because of the much greater detail revealed in Brillouin scattering measurements, it has been necessary to develop in Sec. II a more complete representation of the growth process and the effect of the flux on the carrier drift velocity. Since there have been some conflicting interpretations of light-

FIG. 1. Optical-probe signals as a function of time and position revealing the propagating acoustoelectric domain which appears in GaAs when a high-voltage pulse is applied along a $\langle 110 \rangle$ direction. The time variation in current [$j(t)$] is shown for reference.



scattering^{14,18,19} and birefringence^{11,27} data in CdS, these two techniques are examined in some detail. In Sec. III the experimental methods and some diagnostic experiments are presented. The relationship between scattering intensity and acoustic energy density is discussed in Appendix A. Intense scattering is considered in Appendix B.

The experimental results are divided into two parts: (a) weak-flux data, presented in Sec. IV A, and (b) strong-flux data, presented in Sec. IV B. Additional analysis and discussion of the strong-flux data are presented in Sec. V. The results are summarized in Sec. VI.

II. THEORY

A. Growth from Thermal Background

Because of the strong variation of the acoustoelectric gain^{2,3} with the frequency and propagation direction of the acoustic wave, the application of a high electric field along a $\langle 110 \rangle$ direction in GaAs will result in the amplification of only a small portion of the thermal spectrum of piezoelectrically active shear waves, producing a highly directional beam of flux. Using small-signal theory, let us now examine the frequency bandwidth, angular divergence, and energy content of this beam as a function of time after the field is applied.

In a coordinate system moving with the sound velocity (v_s), the growth of acoustic energy is given by

$$\frac{dU_{\vec{q}}}{dt} = (\alpha - 1/\tau_p)U_{\vec{q}} + C_0U^{\text{th}}, \quad (1)$$

where $U_{\vec{q}}$ is the amplified energy density per unit volume in \vec{q} space, $U^{\text{th}} = kT/(2\pi)^3$ is the equilibrium thermal-energy density, α is the acoustoelectric-gain coefficient, and $1/\tau_p$ is the nonelectronic lattice-attenuation coefficient. For semiconducting material $\alpha = \alpha_0(v_d/v_s - 1)$, where v_d is the electron drift velocity. The second term in Eq. (1) is necessary for detailed balance ($dU_{\vec{q}}/dt = 0$, when $v_d = 0$), which is achieved when $C_0 = \alpha_0 + 1/\tau_p$. Assuming v_d remains constant Eq. (1) can easily be integrated, yielding an excess energy density,

$$\phi_{\vec{q}} = U_{\vec{q}} - U^{\text{th}} = [CkT/(2\pi)^3](e^{\alpha_n t} - 1), \quad (2)$$

where $\alpha_n = \alpha - 1/\tau_p$ and $C = 1 + C_0/\alpha_n$. For $\alpha_n < 0$, $\phi_{\vec{q}}$ saturates at $-CkT/(2\pi)^3$, whereas exponential amplification occurs when $\alpha_n > 0$. Our primary concern here is with the selectivity of this amplification process, which depends upon the nature of α_0 and $1/\tau_p$.

If $ql_e \ll 1$ (where l_e is the electron mean-free path), the Hutson-White theory^{2,3} applies, and

$$\alpha_0 = \frac{e_{ij}^2 e}{\epsilon \rho \mu k T} \left(\frac{2\pi f}{(\omega_s \omega_D)^{1/2}} + \frac{(\omega_s \omega_D)^{1/2}}{2\pi f} \right)^{-2}, \quad (3)$$

where $\omega_s = \sigma/\epsilon$, $\omega_D = ev_s^2/\mu k T$,

and where e_{ij} , e , ϵ , ρ , σ , and f are the appropriate component of the piezoelectric tensor, electron charge, dielectric constant, mass density, conductivity, and frequency of the acoustic wave, respectively. Here the frequency of maximum interaction f_a is given by $(\omega_s \omega_D)^{1/2}/2\pi$. If $ql_e \gg 1$, the power-gain coefficient α_0 is enhanced by a factor $(\frac{1}{2}\pi^{1/2})ql_e$ and $f_a = (3\omega_s \omega_D)^{1/2}/2\pi$.²⁸ Unfortunately, in most of our GaAs material f_a is in the region $ql_e \sim 1$, where one is forced to evaluate α_0 numerically.²⁹ Nevertheless, the basic features of the gain are contained in Eq. (3).

For a wave propagating at an angle δ from the $[110]$ axis, we have

$$e_{ij} = e_{14} \cos^2(2\delta) \quad (4)$$

in the (001) plane, and

$$e_{ij} = e_{14}(3 \cos^3 \delta - 2 \cos \delta) \quad (5)$$

in the $(\bar{1}\bar{1}0)$ plane,² which dominate the angular variation of α . Additional factors occur in the drift-velocity component ($v_d \cos \delta$) and in the sound velocity, which varies approximately as $(1 - 0.85^2)$ in the $(\bar{1}\bar{1}0)$ plane.

Theories³⁰ of phonon-phonon attenuation show $1/\tau_p$ varying as f^2 for $2\pi f \tau_{\text{th}} \ll 1$, and as f for $2\pi f \tau_{\text{th}} \gg 1$, where τ_{th} is the thermal-phonon relaxation time. In GaAs, $(2\pi \tau_{\text{th}})^{-1}$ is approximately 15 GHz at 300 °K,^{31,32} so for the frequencies of interest (see Table I) we expect $1/\tau_p$ to have a frequency dependence somewhat weaker than f^2 . Since $1/\tau_p$ increases monotonically with f , the frequency of maximum net gain f_m will always be less than f_a and will decrease with decreasing drift velocity. Unless otherwise specified, α_n , α , α_0 , and $1/\tau_p$ refer to their respective values along the $[110]$ axis at the frequency of maximum net gain.

The frequency bandwidth $\Delta f_{1/2}$ and the angular bandwidth $\Delta \delta_{1/2}$ of the amplified beam will decrease as the flux grows. An example of this is shown in Fig. 2, where $\Delta f_{1/2}$ and $\Delta \delta_{1/2}$ are given as a function of the growth factor at f_m , the frequency of maximum gain. Most of the reduction in $\Delta f_{1/2}$ and $\Delta \delta_{1/2}$ occurs during the first four-orders-of-magnitude growth. There is little further change from the 10^6 to the 10^{10} growth stage, where $\Delta f_{1/2} \approx 0.4 f_m$ and $\Delta \delta_{1/2} \approx 10^\circ$.

Thus, in calculating the total excess energy density

$$\Phi = \int \phi_{\vec{q}} d\vec{q}, \quad (6)$$

it is only necessary to consider frequencies near f_m and δ 's near 0° . To obtain a tractable solution, we shall assume that for frequencies near f_m , α_n is of the form

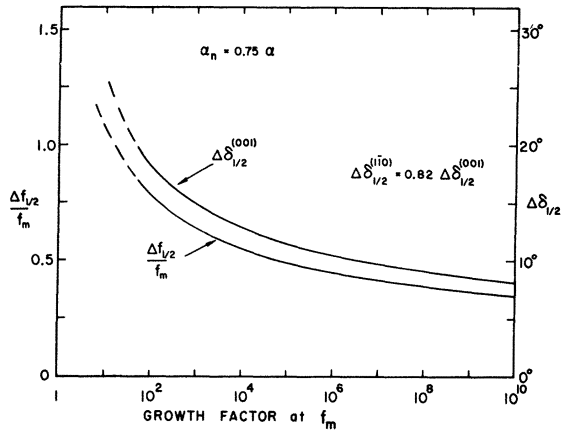


FIG. 2. Relative frequency bandwidth $\Delta f_{1/2}/f_m$ and angular bandwidth $\Delta\delta_{1/2}$ as a function of the acoustic amplification factor at f_m , the frequency of maximum gain.

$$\alpha_n(f) = \alpha_n \left[1 - A \left(\frac{f - f_m}{f_m} \right)^2 \right]$$

An expansion of Eq. (3) gives $A = 1$ for $\alpha \gg 1/\tau_p$. We would not expect A to differ appreciably from unity in any case of interest. In addition, we shall assume α varies as $(1 - B\delta^2)$ about the [110] axis. In most cases, the average angular variation in gain is characterized by $B \approx 6$. Integration of Eq. (6) then yields

$$\Phi = \Phi_0 e^{\alpha_n t}, \quad (7)$$

where

$$\Phi_0 \approx \frac{CkT}{v_s^3} f_m^2 \left[\frac{\pi f_m^2}{A \alpha_n^2} \right]^{1/2} \left\{ \frac{\pi}{B \alpha t} \right\},$$

when $\alpha_n t > 5$. The quantity in the square brackets is the effective-frequency bandwidth, and the term in the curly brackets is the effective cone of propagation. As expected, both decrease with time. Note that the effective-source intensity Φ_0 is a strong function of the frequency of maximum net gain f_m . Since f_a is proportional to the square root of the carrier concentration, Φ_0 should vary roughly as $n^{3/2}$. Thus for samples with high carrier concentration, there is the advantage of a higher starting flux because a *larger volume in \vec{q} space* is available for amplification. However, the larger nonelectronic losses at the higher frequencies usually more than compensate for this.

The spatial distribution of the amplified flux in the sample changes with time, by virtue of the inherent propagating nature of the acoustic waves and the spatially inhomogeneous gain resulting from resistivity inhomogeneities. If we assume the source intensity Φ_0 to be constant and uniform

throughout the sample, then the amplified intensity $\Phi(x, t)$ at a distance x from the cathode at time t after the voltage is applied will be given by

$$\Phi(x, t) = \Phi_0 \exp \int_{x_0}^x \left[\alpha_0(x) \left(\frac{\mu(x) E_0(x)}{v_s} - 1 \right) - \frac{1}{\tau_p} \right] \frac{dx}{v_s}, \quad (8)$$

where $x_0 = 0$ for $x < v_s t$, $x_0 = x - v_s t$ for $x > v_s t$, and where $E_0(x)$ is the Ohmic field at position x . Since $\mu E_0 = v_d$ is usually 5–20 times v_s , and since the product $\alpha_0(x)\mu(x)$ is independent of x , the spatial distribution of flux is controlled solely by $E_0(x)$, hence, by the resistivity profile of the sample.

B. Decrease in Drift Velocity

The rate of momentum transfer³³ from the mobile charge carriers to the amplified acoustic waves is given by

$$eE_d = \frac{ev_d}{\mu} + \frac{1}{nv_s} \int \alpha(\vec{q}) \phi_{\vec{q}} d\vec{q}, \quad (9)$$

where E_d is the average electric field in a region much larger than an acoustic wavelength, but small compared to the spatial distribution of $\phi_{\vec{q}}$. The first term on the right-hand side is just the Ohmic momentum-loss rate, while the second term is the rate of momentum transfer to the acoustic wave. As the flux becomes very intense this additional momentum loss exceeds the Ohmic contribution, resulting in a significant increase in the local resistance and electric field. Assuming constant drift velocity, an integration of the second term in Eq. (9) yields

$$\Phi(t) = \frac{nev_s [E_d(t) - E_0]}{\alpha^e}, \quad (10)$$

where $E_0 = v_d/\mu$ and $\alpha^e \approx \alpha(1 - 2/\alpha t)$ for $\alpha t > 5$. The increase in the effective-gain coefficient α^e with time is due to the shrinkage of the flux distribution about \vec{q}_m . Combining Eqs. (7) and (10) and using the parameters given in Table I, we find that it requires up to 10^8 growth in flux to double the local field. At cryogenic temperatures where f_m and α_0 are generally much larger, the required growth can be much less.

If a constant current supply is fed into the sample, the exponential growth of flux will produce a corresponding growth in voltage across the sample. However, the flux and voltage will not grow indefinitely, as the flux growth would sooner or later be limited by either strong nonlinear losses, excessive Joule heating, or simply by the length of the sample limiting the distance in which flux can grow. In most cases, the voltage supplied by our pulse generators would

not allow constant current to be maintained for even a short period of time in the non-Ohmic regime.

It is relatively easy to maintain constant voltage across a sample; however, in this case we cannot make full use of the above formalism. If v_d is assumed independent of x , Eq. (9) can be integrated over the sample length L , which yields the dependence of v_d on the average acoustic energy density $\bar{\Phi}$ and on the initial Ohmic drift velocity v_0 ,

$$\frac{v_d}{v_s} = \frac{v_0/v_s + \bar{\Phi}/\beta}{1 + \bar{\Phi}/\beta}, \quad (11)$$

where

$$\bar{\Phi}(t) = \frac{1}{\alpha_0 L} \int_0^L \left(\int \alpha_0(\vec{q}) \phi_{\vec{r}}(x, t) d\vec{q} \right) dx$$

and

$$\beta = nev_s^2/\mu\alpha_0.$$

As required, when $\bar{\Phi} \ll \beta$, $v_d = v_0$. However, as $\bar{\Phi}(t)$ increases v_d decreases, and in the limit $\bar{\Phi}(t) \gg \beta$, $v_d = v_s$. The interaction with the flux reduces the drift velocity of the carriers which in turn suppresses the growth of the flux, i. e., a current-flux feedback process occurs. However, β is typically of the order of 10^{-2} J/cm³, and so we should not expect small-signal theory to apply indefinitely in this intense flux regime. Nevertheless, it is instructive to examine some of its predictions in more detail.

Let us assume that the flux is confined to a domain of width d , which propagates down the sample with the velocity of sound. Equation (11) then simplifies to

$$\left(\frac{v_d}{v_s} - 1 \right) = \left(\frac{v_0}{v_s} - 1 \right) \left(1 + \frac{\Phi d}{\beta L} \right)^{-1}, \quad (12)$$

where Φ is the energy density in the domain. If this feedback expression is inserted into the growth equations, one can, in principle, obtain $\Phi(t)$ and $v_d(t)$. However, to simplify the problem, we shall further assume that only one acoustic frequency is present.³⁴ Here, the amplification rate goes to zero when v_d drops to $v_s(1 + 1/\alpha_0\tau_p)$ and gives a saturation drift velocity which is independent of the applied voltage and larger than the sound velocity, a feature characteristic of the acoustoelectric instability.¹⁰

Integration of the growth equation $d\Phi/dt = \alpha_n\Phi$ yields

$$\Phi(t) = \Phi_0 \left(1 - \frac{\Phi(t)}{\Phi_{ss}} \right)^{\alpha_i \tau_p} e^{\alpha_{ni} t}, \quad (13)$$

where

$$\alpha_i = \alpha_0(v_0/v_s - 1), \quad \alpha_{ni} = \alpha_i - 1/\tau_p,$$

and

$$\Phi_{ss} = \left(\frac{v_0}{v_s} - 1 - \frac{1}{\alpha_0\tau_p} \right) \left(\frac{L}{d} \right) \frac{nev_s^2}{\mu} \tau_p. \quad (14)$$

As seen from Eq. (13), the flux grows exponentially when $\Phi \ll \Phi_{ss}$, but eventually approaches the steady-state value given by Eq. (14). In GaAs, v_0/v_s is generally much greater than $1 + 1/\alpha_0\tau_p$, and so Φ_{ss} is essentially independent of α_0 . The total flux in the sample ($\Phi_{ss}d$) increases linearly with v_0 ; and hence with the applied voltage, which is consistent with many of the reported properties of the GaAs domain.^{35,36}

III. EXPERIMENTAL METHODS

A. Brillouin Scattering

Brillouin scattering provides one of the most direct ways of measuring the frequency and intensity of acoustic waves. When a photon of frequency ν and wave vector \vec{k} interacts with a phonon of frequency f and wave vector \vec{q} it experiences a change in frequency and wave vector given by

$$\nu_s = \nu \pm f \quad \text{and} \quad \vec{k}_s = \vec{k} \pm \vec{q},$$

where ν_s and \vec{k}_s are the frequency and wave vector of the scattered photon. If a phonon is created by the interaction, the frequency of the scattered light will be less than that in the incident beam, producing the so-called Stokes component; whereas, if a phonon is absorbed in the process, the scattered light has a higher frequency, the anti-Stokes component. Since f is small compared to ν , it is easily shown that

$$f = (2n_0\nu_s/\lambda_0) \sin \frac{1}{2}\theta',$$

where n_0 is the refractive index of the scattering medium, λ_0 is the optical wavelength in vacuum, and θ' is the angle (in the medium) through which the photon is scattered from the forward direction. The propagation direction of the phonon is given by the perpendicular to the bisector of the scattering angle of the light.

Ordinarily, both the scattering direction and the frequency shift ($\nu - \nu_s$) must be known in order to determine the frequency and propagation direction of the acoustic wave. However, if the velocity of the acoustic wave is known (as is the case with the propagating acoustoelectric domain), we can determine f and \vec{q} simply from the directions of the incident and scattered light beams. Since it is not necessary to measure the frequency shift directly, a highly monochromatic source is not required.

Brillouin scattering from an equilibrium thermal

distribution of phonons in cubic crystals has been examined in detail by Benedek and Fritsch.³⁷ For [110] shear waves with [001] particle motion,

$$I_s^{\text{th}}(\Omega') = I_0 \frac{\pi^2}{v_s^2} \frac{\epsilon^4}{\lambda_0^4} \frac{kT}{\rho} |\vec{\xi}|^2 \Omega' b, \quad (15)$$

with

$$\vec{\xi} = \frac{1}{2} p_{44} \hat{k}_s \times \{ \hat{k}_s \times [\hat{p}_q (\hat{q} \cdot \hat{P}_k) + \hat{q} (\hat{P}_q \cdot \hat{P}_k)] \}, \quad (16)$$

where $I_s^{\text{th}}(\Omega')$ is the intensity of light scattered into the solid angle Ω' , I_0 is the incident intensity b is the light path length through the medium, $\vec{\xi}$ is a vector in the direction of polarization of the scattered beam, \hat{P}_k is a unit vector in the direction of polarization of the incident beam, \hat{P}_q is a unit vector in the direction of polarization of the acoustic wave, \hat{q} and \hat{k}_s are unit vectors in the direction of propagation of the acoustic wave and the scattered photon, respectively, and p_{44} is the appropriate elastooptic coefficient.

The factor kT represents the energy content of a vibrational mode for equipartition of energy throughout the modes. More generally, the energy content is given by $n_q hf$, where n_q is the phonon occupation number. Amplification of acoustic flux from the thermal background produces an increase in n_q above the equilibrium value, and hence a corresponding increase in scattering intensity.

In GaAs p_{44} is about 0.06 at 1.0 μm and decreases with decreasing wavelength.³⁸ Thus, for $\Omega' = 10^{-3}$ sr and $b = 0.5$ mm, we find $I_s^{\text{th}}(\Omega')/I_0 \approx 7 \times 10^{-12}$ at room temperature. The magnitude of the scattering observed from the propagating acoustoelectric domains was in the range from 10^5 to 10^{11} times larger than this, indicating that the acoustic energy density had increased by a corresponding amount

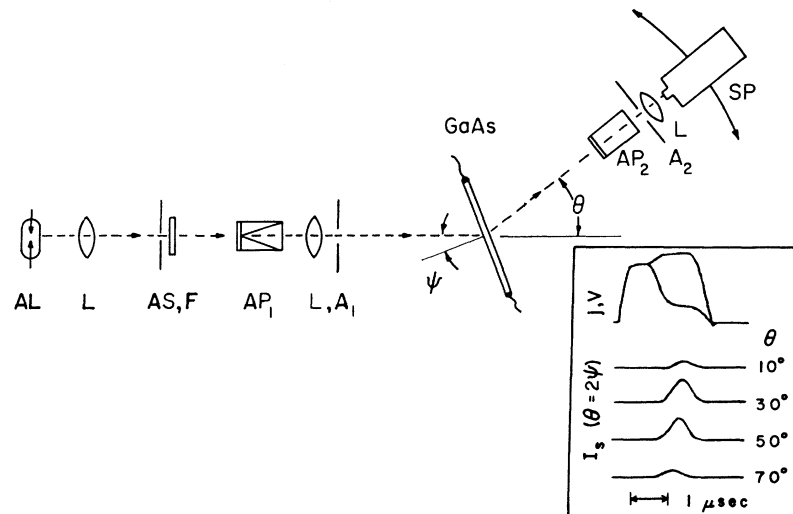
from the thermal value.

Our experimental set up is shown schematically in Fig. 3. Light from a pulsed high-pressure Hg arc lamp (AL) was focused onto an adjustable slit (AS) and then passed through an optical filter (F)³⁹ and an Ahrens prism polarizer (AP₁). The image of the slit was projected onto the GaAs sample, with the incident cone defined by the aperture A₁. The angle of incidence (ψ) was varied by simply rotating the sample. A second Ahrens prism (AP₂) was used to analyze the polarization of the light scattered into an angle θ , with the aperture A₂ defining the collection cone. The light which passed through this aperture was focused onto an EG and G SGD-100 photodiode (SP) and the response displayed on an oscilloscope. The inset in Fig. 3 shows an example of the scattering signals observed at various angles $\theta = 2\psi$, along with oscilloscope traces of the sample current and voltage. Scattered light was detected only during the passage of the acoustoelectric domain through the light beam.

The high refractive index of GaAs ($n_0 \approx 3.5$) severely limits the internal angle at which light enters and leaves the sample, since total internal reflection occurs for angles greater than 17° . Consequently, the internal propagation directions (\hat{k} and \hat{k}_s) are both nearly perpendicular to the [110] axis for all values of θ . The optical path is essentially given by the specimen thickness. Changes in reflectivity with incident angle can be ignored when ψ and $(\theta - \psi)$ are less than 50° . The frequency and propagation direction (in the plane of incidence) of the phonon producing the scattering can be obtained directly from θ and ψ , as

$$f = \frac{2n_0 v_s}{\lambda_0} \sin\left(\frac{1}{2}\left[\sin^{-1} \frac{1}{n_0} \sin(\theta - \psi) + \sin^{-1} \frac{1}{n_0} \sin \psi\right]\right) \quad (17)$$

FIG. 3. Schematic diagram of the apparatus used for detecting Brillouin scattering from acoustoelectric domains in GaAs. Typical examples of scattering signals are shown in the inset along with the current j and voltage V traces.



and

$$\delta = \frac{1}{2} \left(\sin^{-1} \frac{1}{n_0} \sin(\theta - \psi) - \sin^{-1} \frac{1}{n_0} \sin \psi \right). \quad (18)$$

When $\theta = 2\psi$, $\delta = 0$ and Eq. (17) reduces to

$$f = (2v_s/\lambda_0) \sin(\frac{1}{2}\theta). \quad (19)$$

With $\lambda_0 = 1.0 \mu\text{m}$, $2v_s/\lambda_0 = 6.7 \text{ GHz}$, which is the maximum detectable frequency in this scattering configuration.

The aperture placed in front of the detector defines an external collection cone Ω , not the internal cone Ω' , given in Eq. (15). For small cone angles ($< 10^{-2}$ sr was used in these experiments),

$$\Omega' = [\cos(\theta - \psi)/n_0^2] \Omega, \quad (20)$$

which varies slightly as the sample and detector angles are changed.

According to Eq. (16), light scattered by shear waves should exhibit certain distinguishing characteristics which depend strongly upon the polarization and propagation directions of the incident-light beam relative to those of the acoustic wave. The scattering intensity should be a maximum when \hat{k} is perpendicular to the plane of \hat{q} and \hat{P}_q ; whereas, very little scattering should occur when \hat{k} is coplanar with \hat{q} and \hat{P}_q . For [110], [001] shear waves, this means that the scattering intensity is a maximum when the light beam is incident upon the (1 $\bar{1}$ 0) surface and a minimum when incident upon the (001) surface. This was indeed found to be the case for the domain-induced scattering. Our results are summarized in Table II, where the relative intensity and polarization of the scattered light are given for various configurations. Note that the scattered light was polarized either perpendicular or parallel to that of the incident beam depending upon the configuration, which helps identify the shear-wave scattering. The 90° change in polarization isolates it from many types of scattering.

TABLE II. Polarization and intensity of the domain-induced scattering and birefringence signals observed under different optical configurations. The polarization of the scattered signal \hat{P}_{k_s} is given with respect to the incident polarization \hat{P}_k , and the intensities are normalized to the maximum signals.

Configuration	\hat{k} \hat{P}_k	Scattering signal		Birefringence signal ΔI
		\hat{P}_{k_s}	I_s	
[1 $\bar{1}$ 0]	[001]	\perp	1	1
[1 $\bar{1}$ 0]	45° ^a	\parallel	1	< 0.01
[1 $\bar{1}$ 0]	[110]	\perp	1	1
[001]	[110]	\parallel	0.02	< 0.01

^aWith respect to the [001] and [110] directions.

We should also mention that both the Stokes and anti-Stokes scattering signals were observed to have equal intensity, as should be expected for ultrasonic frequencies. For $\delta = 0$, the anti-Stokes configuration is just the mirror image of the Stokes configuration, i. e., θ and ψ are simply changed to $-\theta$ and $-\psi$.

B. Electro-Optic Effect

The application of an electric field to a piezoelectric crystal produces an anisotropic change in the refractive index which is proportional to the field strength (the linear electro-optic effect). Details of this field-induced birefringence in zincblende crystals have been discussed by Namba.⁴⁰ For an electric field in the [110] direction, the maximum phase lag Γ between two components of a plane-polarized light beam occurs when the beam is incident upon the (1 $\bar{1}$ 0) surface, and \hat{P}_k is either parallel to the [110] or the [001] axis. Here,

$$\Gamma = (2\pi/\lambda_0)(n_0^3 r_{14} E b), \quad (21)$$

where b is the optical path length and r_{14} is the electro-optic coefficient. No phase lag occurs if \hat{P}_k is at 45° with respect to the [110] and [001] axes. If the beam is incident upon the (001) surface there is no phase lag, regardless of the direction of \hat{P}_k . In GaAs, r_{14} is about $1.2 \times 10^{-10} \text{ cm/V}$ at $1.0 \mu\text{m}$, and does not appear to be a strong function of wavelength in this region.⁴¹ The intensity ΔI of light transmitted through a system consisting of a GaAs crystal placed between crossed polarizers is given by

$$\Delta I/I_{0\parallel} = \sin^2(\frac{1}{2}\Gamma), \quad (22)$$

where $I_{0\parallel}$ is the transmitted intensity in the absence of the field with parallel polarizers. Birefringence was measured with the apparatus shown in Fig. 3, by simply setting $\theta = 0$.

Ordinarily, electro-optic effect data are simple to interpret. However, when this effect is associated with an acoustoelectric domain, complications arise which have caused some controversy.^{11,27} The high-resistance domain is not only a region of high electric field, but is also a region of very intense acoustic flux. Whether the observed domain-induced birefringence is a field effect or a flux effect must therefore be determined.

The intensity of light detected with crossed polarizers at various angles from the forward direction as the domain passed through the light beam is shown in Fig. 4. Here, $\psi = 15^\circ$ and $\hat{P}_k \parallel [001]$. The detector angle was varied from -50° to 60° , with the analyzer crossed with respect to the polarizer. Brillouin scattering (anti-Stokes) from 1.7-GHz phonons

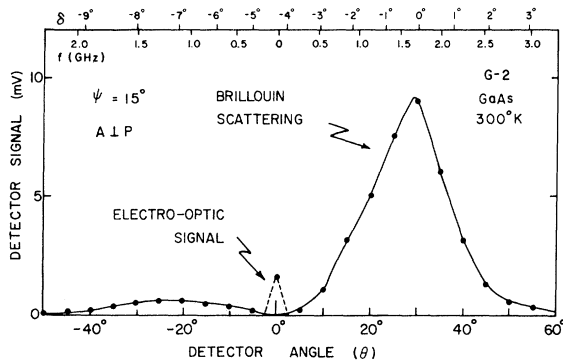


FIG. 4. Intensity of the domain-induced optical signal (detected with crossed polarizers) as a function of angle θ from the forward direction. Brillouin scattering is responsible for all but that at $\theta = 0^\circ$, which is due to the electro-optic effect. The frequency f and propagation angle δ of the acoustic waves producing the scattering are given at the top of the figure.

propagating along the sample axis is responsible for the intensity peak at 30° . The broad intensity distribution centered at about -25° is a result of Brillouin scattering (Stokes) from off-axis flux, e. g., 1.7-GHz flux moving -8.5° off axis scatters light at -35° . The frequency and propagation direction of the phonons responsible for scattering at various angles is given at the top of Fig. 4. The ratio of the intensity at 30° to that at -35° is about 20:1, which is to be expected from our knowledge of the amplified flux cone (see Sec. IV). As θ approaches 0° the signal drops off rapidly. However, at $\theta = 0^\circ$ we find a relatively large signal, over 10 times that observed at $\theta = \pm 5^\circ$. This could not be caused by two successive Brillouin scatterings (see Appendix B), since light scattered twice would have the same polarization as the incident beam, and therefore would not be detected. The intensity of this signal at 0° corresponds to $0.01 I_{0m}$. If we assume this is due to the electro-optic effect, we obtain a field of about 13 kV/cm, which is in good agreement with the field (15 ± 3 kV/cm) estimated from the current modulation and the domain width.

Severe complications arise when the intensity of the low-frequency (< 0.2 GHz) acoustic waves becomes large. Small-angle scattering produced by these shear waves will throw perpendicularly polarized light into the finite collection aperture, through analyzing prism, and obscure the birefringence signal. This could easily lead one to believe that the domain-induced "birefringence" was the result of the photoelastic effect, exhibiting the properties of low-frequency acoustic waves.

The strong polarization dependence found for the domain signal (see Table II) is in excellent agreement with that discussed above for the electro-

optic effect. With the light beam incident upon the $(1\bar{1}0)$ surface, large signals were found with the incident beam polarized either along the $[001]$ or along the $[110]$ axis, but with \hat{P}_k at 45° with respect to these axes, no signal was detected. Also, no signal was observed with the light beam entering the sample along the $[001]$ direction.

If the phase lag is small, the electro-optic signal is proportional to E^2 . Consistent with this is our observation that the domain-induced birefringence signal was proportional to the square of the voltage across the domain in a sample where the domain width changed very little during growth. When the voltage across the sample was rapidly cut off, the birefringence signal dropped sharply to zero, while the Brillouin-scattering signals persisted for some time (see Fig. 12). We therefore feel that the observed domain-induced birefringence signal is due to the electro-optic effect and is only *indirectly* related to the acoustic flux. This enables us to precisely correlate the growth of the electric field in the propagating domain with the acoustic flux level, since the *same* optical probe is used for both the birefringence and the Brillouin-scattering measurements.

IV. RESULTS

A. Weak-Flux Regime

In this section we present the properties of the amplified acoustic waves at the earliest detectable growth stages, prior to the occurrence of strong non-Ohmic effects. Here the intensity, growth rate, and the spectral, angular, and spatial distributions of the flux will be examined and compared to the predictions of small-signal theory.

Growth Rate

The best test of the growth was provided by Brillouin-scattering measurements on samples from ingot *R*, where 3.1-GHz acoustic waves produced the most intense scattering in the initial stages of detection. The intensity of these waves as a function of time is shown in Fig. 5 at three representative applied fields along with the associated current traces. The energy density relative to the thermal energy density U^{th} is given by the quantity I_s/I_s^{th} — the ratio of measured scattering intensity to that calculated for a thermal distribution. The growth is exponential in the observable range (solid lines) from 10^6 to $10^8 U^{\text{th}}$. The fact that I_s/I_s^{th} extrapolates (dashed lines) back to unity at the onset of the voltage pulse, attests to the applicability of the simple gain theory and the scattering relation given by Eq. (15). The decrease in growth rate and the onset of flux saturation at $\sim 2 \times 10^8 U^{\text{th}}$ signified the end of the simple exponential-growth range.

The slope of each growth curve gives the net gain coefficient α_n . A plot of α_n versus $(v_d/v_s - 1)$ ⁴² (see inset in Fig. 5) yields the parameters α_0 and $1/\tau_p$. At 3.1 GHz, we find $1/\tau_p \approx 2.5 \times 10^6 \text{ sec}^{-1}$, which corresponds to an $f^{1.7}$ extrapolation of Keller and Abeles's⁴³ attenuation value at 0.63 GHz. This frequency dependence is to be expected for frequencies in this range.³⁰ In addition, we find $\alpha_0 = 8 \pm 1 \times 10^5 \text{ sec}^{-1}$, which is reasonably consistent with the Hutson-White (HW) theory,^{2,3} according to which $(\alpha_0)_{\text{HW}} = 5.6 \pm 0.6 \times 10^5 \text{ sec}^{-1}$ based on an electromechanical coupling constant $K^2 = e_{14}^2/\epsilon c_{44} = 3.7 \pm 0.3 \times 10^{-3}$.⁴⁴ The Hutson-White expression should not be completely applicable here where $ql_e = 0.6$. Jacobini and Prohovsky's (JP)²⁹ calculation, applicable for all values of ql_e , gives an $(\alpha_0)_{\text{JP}} = 1.3(\alpha_0)_{\text{HW}}$ at 3.1 GHz for the present sample parameters, which is in better agreement with the experimentally obtained value.

Frequency Distribution

The amplified spectrum at a time 2.5 μsec after the application of the field (720 V/cm) is shown by the data points in Fig. 6, along with the energy distribution of shear waves in thermal equilibrium, calculated according to the Debye theory for a 1-

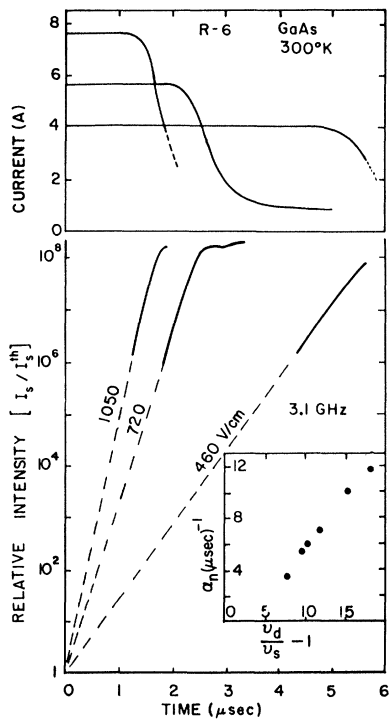


FIG. 5. Relative scattering intensity at 3.1 GHz as a function of time for three different applied fields. The current traces are shown for reference. The inset shows the net-gain coefficient α_n as a function of $(v_d/v_s - 1)$.

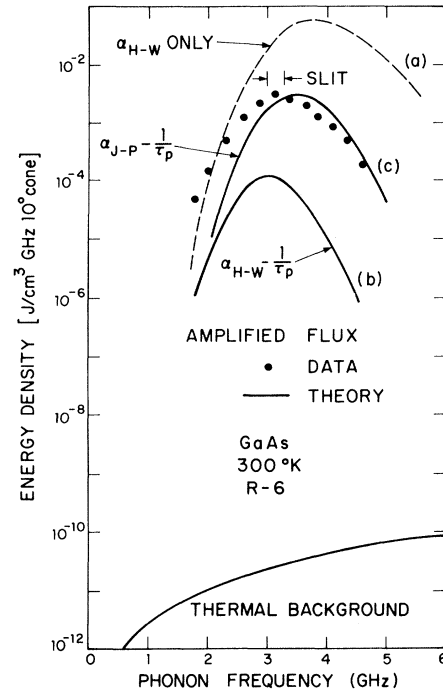


FIG. 6. Frequency distribution of the amplified acoustic energy density at an early growth stage. The solid lines represent the thermal background intensity and the theoretical amplified distributions (see discussion in text).

GHz bandwidth and 10° propagation cone. The amplified energy density is obtained by simply multiplying the thermal energy density by the scattering factor I_s/I_s^{th} . The amplified spectrum calculated using $(\alpha_0)_{\text{HW}}$ is given by curve (a). The importance of taking lattice losses into account ($1/\tau_p \sim f^{1.7}$ was used in the discussion above) is demonstrated by curve (b); i. e., lattice losses drop the amplified energy density by a factor of 300 and produce a small downward shift in the frequency of maximum intensity. At this stage the theory gives 30 times smaller flux than was experimentally observed. But this discrepancy is *extremely* sensitive to the magnitude of α_0 , and is nearly eliminated by using the more appropriate $(\alpha_0)_{\text{JP}}$ as is shown by curve (c). The observed bandwidth of the spectrum (1.2 GHz) was easily resolved and compares well with the 1.1 GHz predicted.

At this stage in acoustic growth the peak excess electric field in the domain ($E_d - E_0$) was about 1.6 kV/cm. For this excess field, Eq. (10) yields a *total* acoustic energy density of about 10^{-2} J/cm^3 , which also agrees with our measurements.

The initial frequency distribution in higher-carrier-concentration samples ($n \approx 5 \times 10^{15} \text{ cm}^{-3}$) was

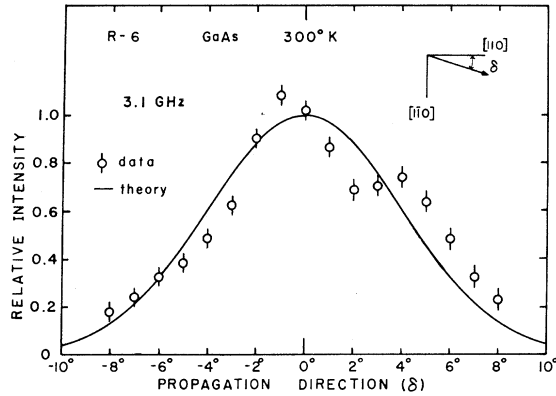


FIG. 7. Angular distribution in the (001) plane of the 3.1-GHz flux at the 10^8 growth stage. The solid line represents the theoretical distribution.

also examined. Here, however, no scattering could be detected until after the current dropped nearly to its saturation value, about $1 \mu\text{sec}$ after strong non-Ohmic effects began to occur. At this stage, the frequency of maximum energy density was *greater than* 5 GHz. Flux of 6 GHz (140° scattering) could easily be observed at this initial detection stage. However, the expected frequencies of maximum acoustoelectric gain in these samples are in the range of 12–15 GHz, which could not be detected with our Brillouin-scattering probe. Since a large local field was obviously built up in the domain *before* scattering could be detected (electro-optic signals were observed before scattering signals), it is not unreasonable to assume that high-frequency flux produced the initial non-Ohmic effects.

Angular Distribution

The angular distribution [in the (001) plane] of 3.1-GHz flux at the 10^8 growth stage is shown in Fig. 7, along with the theoretical distribution (solid line) calculated according to the discussion in Sec. II. As expected the observed distribution is centered along the [110] axis. The measured cone angle ($\sim 10^\circ$) is also in good agreement with theory. Measurements in the higher-carrier-concentration samples gave essentially the same results. The propagation cones of the initially detected flux (4 GHz and above) ranged from 7° to 10° . We should note, however, that in Sec. II, we tacitly assumed the acoustic waves striking the surfaces of the sample to be 100% specularly reflected. If this is not the case, then for very-thin samples (the high-carrier-concentration samples were $< 0.2 \text{ mm}$ thick) the cone angle should be somewhat less than calculated.

Spatial Distribution

The spatial distribution of the initially amplified flux was found to be a strong function of the resistivity profile of the sample. If relatively higher Ohmic resistance regions were in the upstream half of the sample, a traveling domain was formed, whereas if they were located in the downstream half, a relatively stationary domain at the anode appeared. These observations are consistent with Eq. (8). In Fig. 8, a comparison between the measured domain shape (at 3.1 GHz) and that calculated from Eq. (8) using the resistivity profile $\rho(x)$ obtained from photoconductivity data²³ is made. The predicted asymmetric shape is clearly shown by the Brillouin scattering data. The arrow in the figure (labeled $v_s t$) represents the distance through which flux, originating from the cathode, would have traveled in time t . So here the flux in the *peak* of the domain originated near the cathode. However, not all propagating domains were found to “originate” from the cathode; the specific origin varied with the resistivity profile. Large inhomogeneities are not necessary to produce distinct propagating domains; 10% inhomogeneity is sufficient. In CdS, where the initial drift velocity is generally only slightly larger than v_s , the effects of inhomogeneities should be, and are,²² much stronger.

B. Strong-Flux Regime

As the flux becomes very intense, the momentum-transfer rate from the mobile carriers to the acoustic waves exceeds the Ohmic loss rate and causes large increases in the local field within the domain. At about this time, pronounced changes in the spectral and spatial distributions of the flux are observed. Since all these experiments were subject to the constant-voltage constraint, as the localized

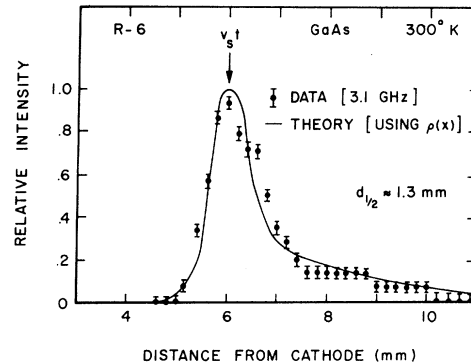


FIG. 8. Spatial distribution of the 3.1-GHz flux at the 10^7 growth stage. The solid line is the calculated distribution, using the resistivity profile $\rho(x)$ to determine the spatial dependence of the gain.

acoustoelectric field grew, the current dropped.

Extrapolating from small-signal theory, we would expect a decrease in gain to occur when the current drops, and since this produces a downward shift in the frequency of maximum *net* gain, we would anticipate a small, gradual down-shift at the acoustic spectrum. However, in contrast to this, we find that the strong-flux regime is characterized by a large *rapid* down shift in frequency.⁴⁵ An example of the Brillouin scattering signals observed when the acoustic intensity in the domain becomes very strong is shown in Fig. 9, along with the current and voltage traces. At this stage the frequency of maximum scattering intensity is about 0.4 GHz, almost $\frac{1}{10}$ the initial frequency of maximum intensity. The lower trace in Fig. 9 shows the transmitted light signal (I_t). At this flux intensity, over 85% of the incident beam is scattered, mainly by *low-frequency* acoustic waves. This intense scattering produces some distortion, as can be seen by the dip in the center of the 10° scattering signal. As shown in Appendix B, the acoustic intensity is given by the ratio I_s/I_t . The dip is due to the decrease in I_t rather than an actual decrease in acoustic energy in the center of the domain. The small scattering signal occurring about $2.5 \mu\text{sec}$ after the main signal for $\theta = 5^\circ$ and 10° is also caused by the domain, but after its reflection from the anode. This is only observable at low frequencies, where lattice attenuation is small. Note in Fig. 9(a) that after the voltage is cut off the current persists for a period of time at a much reduced value. If the persistent current corresponds to an electron drift velocity equal to the sound velocity,⁴⁶ then clearly the saturation drift velocity just before cut off is much

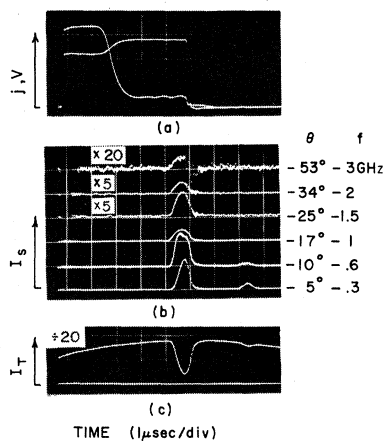


FIG. 9. Oscilloscope display of the scattering signals observed near the anode of sample R-6. The transmitted light signal I_t ($\psi = 0^\circ$), and the current and voltage traces are also shown.

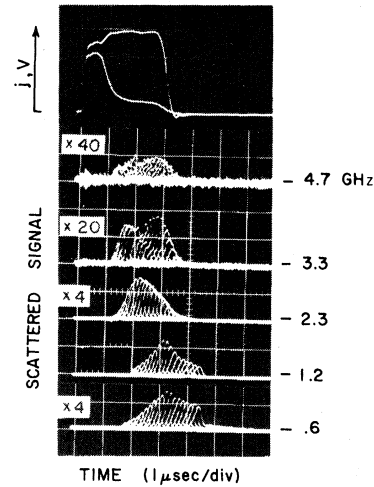


FIG. 10. Oscilloscope display of the scattering signals observed at successive positions along sample O-2 for five different acoustic frequencies. The current and voltage traces are also shown.

larger than the sound velocity, in contrast to CdS.²⁶

Growth and Decay Rates

An example of the evolution of various frequency components in a higher-carrier-concentration sample (O-2) is shown in Fig. 10. The multiple traces in the photographs represent scattering signals taken at successive positions down the sample. The high-frequency components (4.7 and 3.3 GHz) grow rapidly to a "steady-state" level, appear to decrease slightly, and then continue to grow again at a much slower rate. This two-stage growth pattern has been consistently observed at high frequencies in all samples examined. The intermediate-frequency component (2.3 GHz) grows more slowly, and attains a steady-state level after about $2 \mu\text{sec}$. The decrease in signal observed before the end of the voltage pulse is caused by depletion of the transmitted beam by intense scattering, and does not represent an actual decrease in acoustic intensity. The lowest frequencies (1.2 and 0.6 GHz) appear quite late, and grow slowly. Growth continues to the very end of the voltage pulse, with no sign of reaching a steady state. In the final stage, I_s is maximum at frequencies $\frac{1}{10}$ the initial frequency of maximum gain ($\sim 15 \text{ GHz}$ in this case).

More detailed growth patterns are shown in Fig. 11 for sample R-6, where the frequency of maximum intensity was initially about 3 GHz. The acoustic energy density (normalized to a 1-GHz bandwidth and 10° propagation cone) as a function of time is presented for seven different frequencies. Also shown is the excess electric field in the domain $E_d - E_0$ (dotted line) obtained from

of *phonon-phonon* interactions. Since the parametric-conversion coefficient⁴⁷ is essentially independent of drift velocity for $v_d < 10v_s$, any frequency down-conversion would continue after the voltage drop, producing net gain at the lower frequencies for a brief period of time. After the various frequencies reach their peak intensities they exhibit rather complicated decay patterns, not the simple exponential rates that one might expect. Note, in particular, the 0.6-GHz component, which shows a very rapid initial decay rate followed by a much slower decay. This slow decay is in good agreement with that measured by Keller and Abeles.⁴³ From such data we find that $1/\tau_p$ varies roughly as $f^{1.7}$ in this region.

Spectral Composition

The deviation from small-signal theory is most obvious from the strong-flux spectrum; an example of which is shown in Fig. 13 at four growth stages in sample *R-5*. The inset shows the time variation of the drift velocity, with the dashed line representing the saturation drift velocity obtained by applying a still higher voltage pulse to the sample. Stage

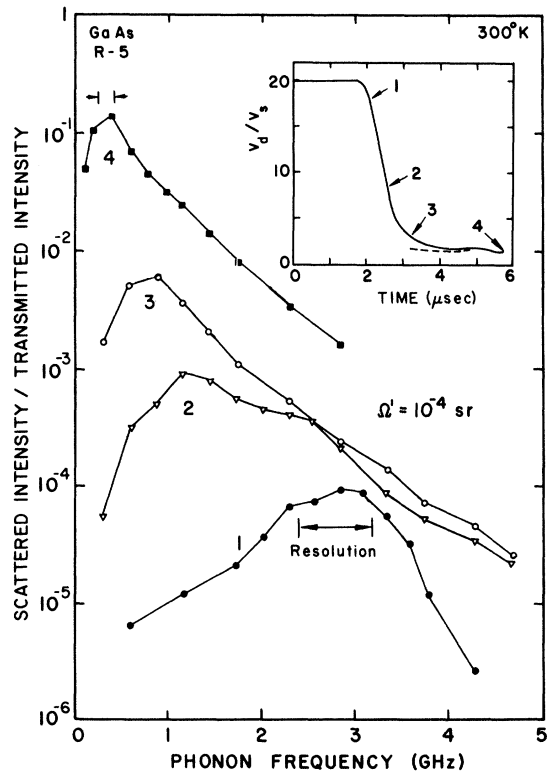


FIG. 13. Frequency spectra of the relative scattering intensity at four stages in growth. The drift velocity as a function of time is shown in the inset, with the dashed line corresponding to the saturation drift velocity.

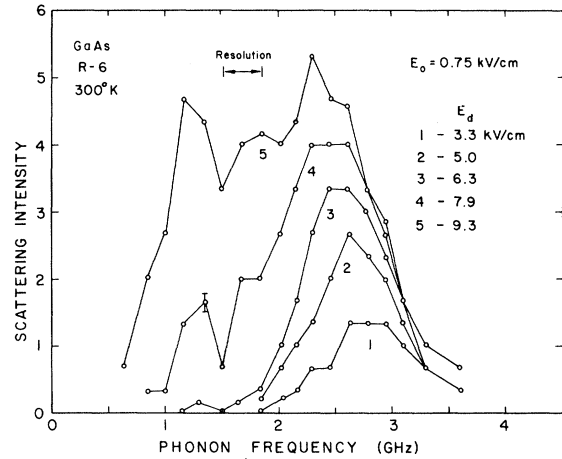


FIG. 14. Frequency spectra of the scattering signals at successive 0.1- μ sec intervals in sample *R-6*, showing the initial deviation from the small signal spectrum.

(1) is in reasonable agreement with small-signal theory. As the current drops, the distribution broadens on the low-frequency side. Most of this down-shift occurs during the first microsecond of the current drop when the frequency of maximum scattering intensity⁴⁸ shifts from over 3 to less than 1 GHz.

In the very-strong-flux regime, the spectrum has practically no fine structure (at least none that can be seen with 0.2-GHz resolution), being characterized by an intensity peak, with a monotonic drop on both sides. However, a close examination of stage (2) suggested some apparent fine structure on the low-frequency side of the peak, which was further investigated.

A more detailed study of the spectrum at the early stages is shown in Fig. 14 at successive 0.1- μ sec intervals. The gradual shift in the peak with time can at least partly be explained from small-signal theory. However, the formation of a second peak at about $\frac{1}{2}$ the frequency of the first (observed in all samples investigated) is a clear deviation from small-signal theory. The position of this peak strongly suggests that subharmonic frequency conversion may be an important factor here.⁴⁹

Angular Composition

In general, the angular distribution of the acoustic waves in the strong-flux regime differs little from that initially observed in the weak-flux regime. The cone of the high-frequency flux appears to shrink slightly (1° or 2°), and the distributions of the low-frequency waves appear much the same as that of the high frequency. The angular distribution of the 1.2-GHz flux in sample *R-6* is shown in Fig. 15 at two stages in growth, an early stage in

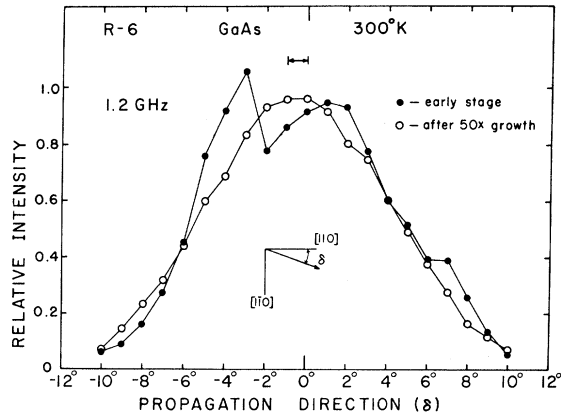


FIG. 15. Angular distribution in the (001) plane of the 1.2-GHz flux at two different stages in growth.

detection and a later stage (after $50\times$ growth). The half-widths of both distributions are about 11° (slightly larger than observed at 3.1 GHz) and both are centered along the [110] axis. However, at the early stage two peaks appear at 1° and -3° . The appearance of these two peaks is indicative of subharmonic conversion. Because of dispersion,² momentum is conserved only when the subharmonic components propagate at $\sim 4^\circ$ with respect to each other. These peaks are no longer present in the later stage, where the distribution has a Gaussian character.

Spatial Distribution

The spatial distributions of the 3.1- and 1.5-GHz components are shown in Fig. 16 at the stage when the scattering intensity from the 1.5-GHz waves was about $\frac{1}{2}$ that at 3.1 GHz. In the weak-flux regime, 1.5-GHz waves were not detectable. Here the 3.1-GHz domain has a half-width of about 2.0 mm and is slightly asymmetric, whereas the 1.5-GHz domain is only 0.8 mm wide. Such a narrow domain cannot be explained by inhomogeneities. At this stage the half-width of the 3.1-GHz domain is significantly *larger* than it was at an earlier stage in growth (see Fig. 8). As the 1.5-GHz waves grow more intense, this domain also broadens (to a half-width of 1.5 mm), while a narrow domain of lower-frequency (~ 0.7 -GHz) waves grows up in the center of it. Throughout the strong-flux regime, narrow domains of successively lower frequencies appear and broaden to ~ 1.5 mm as they become more intense. The process appears to be the result of a siphoning off of the most intense part of the domain at a high frequency to form a narrow domain at a lower frequency.⁵⁰ In other words, parametric down-conversion could explain the evolution of domains at the various frequencies.

V. ANALYSIS AND DISCUSSION

A. Parametric Frequency Conversion

The continued growth at low frequencies after the voltage was cut off (see Fig. 12), the appearance of a second peak in the spectrum near $\frac{1}{2}f_m$ (see Fig. 14), the two peaks in the angular distribution at low frequencies (see Fig. 15), and the narrow domains initially formed at low frequencies (see Fig. 16) are all consistent with the idea of parametric subharmonic conversion being an important process in the strong-flux regime. To see if this is plausible, we shall analyze the growth patterns at the fundamental frequency (3.1 GHz) and its subharmonic (1.5 GHz). The normalized scattering intensities as a function of time for these two components is shown by the solid lines in Fig. 17. The dashed lines represent the growth predicted by small-signal theory. Although the initial growth at 3.1 GHz is in good agreement with this theory, the growth at 1.5 GHz is about three times faster than expected, and here the observed intensity ratio I_s/I_s^{th} does not extrapolate (double-dashed line) to unity at $t=0$, the onset of the voltage pulse. The initial growth rate at 1.5 GHz is over 50% larger than the initial rate at 3.1 GHz. The latter begins to decrease at about the time the 1.5-GHz flux is detected.

If the rapid delayed growth at 1.5 GHz and the decreased growth rate at 3.1 GHz is a consequence of parametric down-conversion, then the difference ($\Delta\alpha_n$) between the observed growth rate of 12×10^6 sec^{-1} at 1.5 GHz and that predicted by small-signal theory (4.3×10^6 sec^{-1}) must be equal to the para-

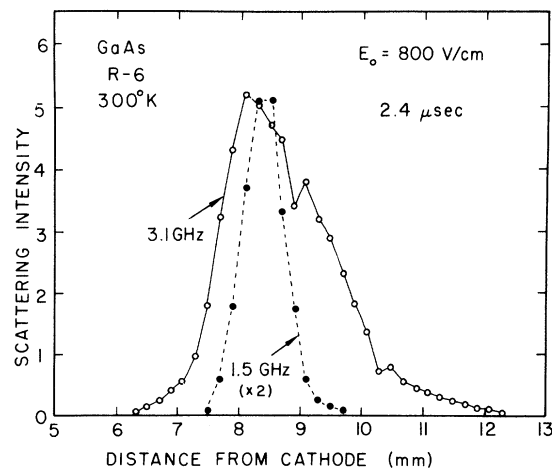


FIG. 16. Spatial distributions of the scattering signals at 3.1 and 1.5 GHz at the stage when the 1.5 GHz is first detected.

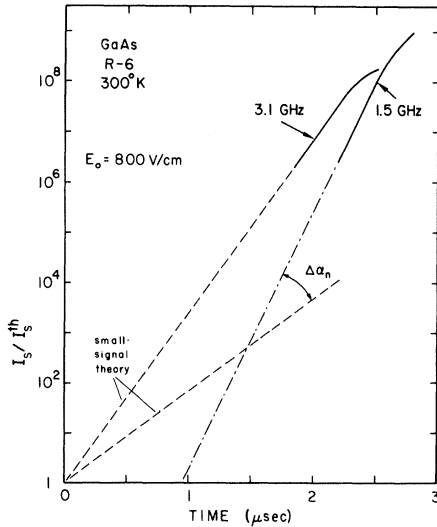


FIG. 17. Initial growth of the 3.1- and 1.5-GHz scattering signals. The dashed lines represent the theoretical small-signal growths at these frequencies.

metric-conversion coefficient. A calculation based on a simple two-frequency model of parametric subharmonic conversion,⁴⁷ indicates that the strain amplitude of the “pump” frequency (3 GHz) should be 4×10^{-4} to produce the required growth at the “signal” frequency (1.5 GHz). Although the rms strain amplitude ($\sim 6 \times 10^{-4}$) calculated from the measured energy density is larger than this, it is not obvious how much of the 1-GHz band centered around 3 GHz is instrumental in conversion to 1.5 GHz. A more general theory which takes into account the distribution of frequencies and phases would be of great value here. Nevertheless, the order-of-magnitude agreement with the simple theory does indicate that the intensity of the acoustic waves in the domain is sufficient for parametric down-conversion to be an important process.

Additional experimental evidence for subharmonic frequency conversion in acoustoelectric domains was obtained from studies of the current-noise spectrum⁵¹ and microwave-emission spectrum⁵² in GaAs. The latter study also indicated that frequency up-conversion occurs at still later growth stages.

B. Flux-Dependent Acoustoelectric Gain

The momentum-transfer relation, Eq. (9), is expected to be valid even in the strong-flux regime. Since this relation involves only the electron-phonon interaction, it provides a means of separating this interaction from the phonon-phonon interactions. Equation (10) defines an average effective-gain coefficient (α^e); all quantities in this equation can be obtained experimentally, E_d from electro-optic data and Φ from Brillouin scattering data. Although it

is usually more meaningful to examine the coefficient α_0^e , here there has been some controversy as $v_d \neq \mu E_d$ in the non-Ohmic regime. According to the v_d model¹⁰ (which we have used throughout our previous discussions), $\alpha^e = \alpha_0^e (v_d/v_s - 1)$, whereas in the μE_d model,⁵³ $\alpha^e = \alpha_0^e (\mu E_d/v_s - 1)$. Although both models are obviously oversimplified, it will be instructive to compare their relative merits. Also of interest will be a comparison of the effective-gain coefficient with the average value obtained from small-signal theory,

$$\langle \alpha_{0,ss} \rangle = \frac{\sum \alpha_{0,ss}(f) \phi(f)}{\sum \phi(f)}, \quad (23)$$

where $\alpha_{0,ss}(f)$ is the small-signal gain coefficient and $\phi(f)$ is the measured intensity at frequency f .

The effective-gain coefficients α^e and α_0^e , and the normalized coefficients $\alpha_0^e / \langle \alpha_{0,ss} \rangle$ (using the v_d and μE_d models) are shown in Fig. 18 as a function of domain field in the *intermediate* growth regime. The total excess energy density Φ grows from about 10^{-2} J/cm³ at $E_d = 3$ kV/cm to about 10^{-1} J/cm³ at $E_d = 13$ kV/cm. Beyond this stage, corrections for the intense scattering became too large to allow accurate comparison. The initial applied field E_0 was about 0.8 kV/cm, and the field in the domain saturated at about 16 kV/cm. Note that as the domain field grows and v_d decreases, α^e decreases, indicating that the gain is controlled by the drift velocity, not the field. However, according to the v_d model, α_0^e increases as the flux grows. The ratio $\alpha_0^e / \langle \alpha_{0,ss} \rangle$ shows an even greater increase as the flux builds up, which is to be expected, since $\langle \alpha_{0,ss} \rangle$ decreases with increasing percentage of flux at low frequencies where $\alpha_{0,ss}$ is very small. In the region $E_d < 3$ kV/cm, both α^e and α_0^e remain relatively constant, since here the growth of the field

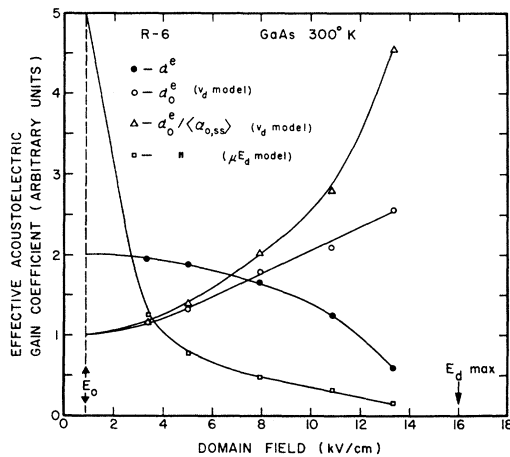


FIG. 18. Effective-gain coefficients as a function of domain field in the intermediate growth regime.

parallels the flux growth (see Fig. 11) and the current is close to the Ohmic value. The μE_d model gives an $\alpha_0^e / \langle \alpha_{0,ss} \rangle$ which decreases rapidly with E_d , occurring as soon as the field in the domain becomes non-Ohmic. Obviously, this model cannot be used as an extrapolation of small-signal theory.⁵⁴ We believe the v_d model provides a much better base for discussion of the strong-flux effects.

In terms of the v_d model, the acoustoelectric gain is enhanced in the strong-flux regime. However, it is not obvious whether the v_d form of the gain expression is no longer valid or whether the coefficient $\alpha_0(f)$ is changed,⁵⁵ or both. If it were only $\alpha_0(f)$ that is to be modified, then it should be noted that the *average* gain coefficient α_0^e in the strong-flux regime is greater than the *maximum* small-signal gain coefficient. In this case, the gain may be equally enhanced at all frequencies or it may be greatly enhanced in only part of the spectrum. These possibilities cannot be distinguished from the growth rates at the various frequencies, since other processes (frequency conversion) must also be considered.

C. Feedback Upon Current

The observed current pattern and that calculated from the small-signal single-frequency model are compared in Fig. 19. The solid lines represent the theoretical acoustic intensity and drift velocity. The former is obtained from Eq. (13) using $\alpha_0 = 7.5 \times 10^5 \text{ sec}^{-1}$ and $\tau_p = 0.4 \text{ } \mu\text{sec}$ (both consistent with our results in Sec. IV A), and an effective thermal-background source ($\Phi_0 = 10^{-10} \text{ J/cm}^3$) calculated

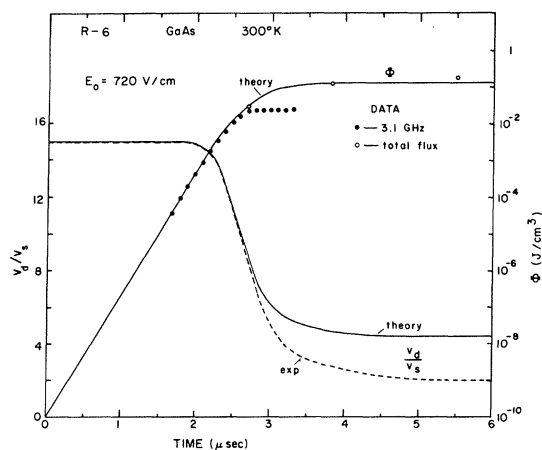


FIG. 19. Variation of drift velocity and acoustic energy density with time. The solid lines represent the time variation calculated from the small-signal single-frequency model. Both the total acoustic energy density and that contained in a 1.2-GHz band centered at 3.1 GHz are shown.

from Eq. (7) at $t = 2.5 \text{ } \mu\text{sec}$. The drift velocity was then obtained from Eq. (12). The dashed curve in Fig. 19 represents the experimental drift velocity, and the data points show both the total energy density and that in a 1.2-GHz band centered at 3.1 GHz. The former deviates from the latter when the acoustic spectrum spreads to low frequencies. The transition of the drift velocity from the Ohmic value ($15v_s$) to its saturation value ($\approx 2v_s$) takes place over a relatively long period of time, at least $3 \text{ } \mu\text{sec}$. The tail-end of this decay is particularly slow. Only during the last $1 \text{ } \mu\text{sec}$ of the domain transit is the drift velocity close to saturation.

From the onset of the voltage pulse through the first 50% drop in current, there is good agreement with this simple model. During this period a single frequency (3.1 GHz) provides a good representation of the total flux. At $t = 2.7 \text{ } \mu\text{sec}$, both the growth of the 3.1-GHz flux and the drop in current begin to deviate from the theoretical curves. Thereafter, the 3.1-GHz waves grow slower than predicted. However, the total flux in the sample becomes somewhat *larger* and the current drops considerably *lower* than predicted. To account for the low-saturation drift velocity on the basis of Eq. (11) would require that the product $\alpha_0^e \Phi$ be much larger than given by small-signal theory, which is consistent with our analysis in the preceding section.

It is obvious that this small-signal single-frequency model breaks down in the very-strong-flux regime; however, the model is reasonably accurate up to the first 50% drop in current and provides a good qualitative picture of the process as a whole.⁵⁶ The simplicity of the model makes it very useful for discussing and evaluating strong-flux effects. On the basis of this single-frequency model, the gradual decay of the drift velocity can be interpreted as due to a gradual increase in the product $\alpha_0 \tau_p$. The extension of the acoustic spectrum to low frequencies and the change in α_0^e discussed in the preceding section are consistent with such an increase.

D. Is There a Steady-State Domain?

Although the acoustic growth rate decreased as the domain neared the anode, no steady-state condition was observed. The lowest frequencies ($< 0.5 \text{ GHz}$) were still growing rapidly as late as $4 \text{ } \mu\text{sec}$ after the initial drop in current. Higher frequencies were also growing, but at a very slow rate (see Fig. 11). The total amplified energy density near the anode was about 0.5 J/cm^3 . Although small compared to the total thermal energy density ($\sim 300 \text{ J/cm}^3$ at room temperature), this energy is present in a different form, being a polarized

beam ($\sim 10^5$ W/cm²) of piezoelectrically active shear waves of many different frequencies and phases. Over most of the spectral range the energy density varied monotonically, increasing by a factor of 100 from 6 to 0.6 GHz. Conceivably, one important factor here may be the phonon lifetime, which for $\tau_p \sim f^{-1.7}$ would vary by 50 over this range. The prolonged storage of flux at low frequencies could help account for their prominence.

We cannot say when the acoustic spectrum will reach a steady state, if indeed such a situation can exist. Certainly, one should not expect the domain to be acoustically stable while the parameter $(v_d/v_s - 1)$ is decreasing.⁵⁷ Only for a very short period of time at the end of the 22-mm transit of the domain was this parameter reasonably constant (see Fig. 19). However, here the over-all growth of the acoustic flux was considerably less than in the earlier stages, suggesting that if the flux were allowed to travel a few more millimeters, a steady state may be reached.

The electric field in the domain, on the other hand, reaches a steady-state value at a relatively early stage (see Fig. 11). In most of our samples⁵⁸ we found a steady-state field of about 15 kV/cm. Similar effects have been observed at 77 °K, where the field saturates at a much lower value (≈ 4 kV/cm).^{35,36} This field saturation has been shown⁵⁹ to be an inherent feature of the intense flux, suggesting that the core of the domain is a region of very strong acoustic losses. Most likely, the acoustic frequencies which interact strongest with the electrons are being parametrically converted to other frequencies. This could either be due to up-conversion or down-conversion, or both. Since the frequency of maximum acoustoelectric gain is not known in the strong-flux regime, it is not possible to say which process would be the more efficient one.

VI. SUMMARY

All observed properties of the acoustic flux initially detected in acoustoelectric domains in GaAs have been found consistent with linear amplification (according to small-signal theory) of shear waves present in the equilibrium thermal background. This covers such properties as intensity, growth rate, frequency distribution, angular distribution, and spatial distribution, when the amplified acoustic energy density is less than $\sim 10^{-2}$ J/cm³, representing almost eight orders-of-magnitude growth from the thermal intensity.

As the waves grow more intense, dramatic changes in the spectral and spatial distributions begin to take place. Parametric down-conversion of acoustic frequencies appears to be the primary cause of the departure from small-signal theory.

As the current drops, the coupling between the electrons and the shear waves decreases, but not as rapidly as the factor $(v_d/v_s - 1)$ contained in the small-signal gain coefficient. Thus, at least two nonlinear effects enter into the amplification process long before current saturation.

The acoustic energy density grows continually throughout the one-way transit of the domain. However, near the end of the sample, when the energy density approaches 1 J/cm³, the rate of growth slows down considerably. In contrast to this, the peak electric field in the domain reaches a steady-state value of ~ 15 kV/cm at a relatively early stage. During the last few microseconds of transit, both the shape of the domain and its frequency composition appear to be controlled almost entirely by nonlinear processes. Although parametric frequency up-conversion and down-conversion and flux-dependent acoustoelectric gain all seem to contribute, it has not been possible to judge their relative importance. The very high intensity and noisy incoherent character of these shear waves, coupled with the fact that the drift velocity saturates well above the sound velocity, presents an extremely complex problem. It is hoped that this study of the evolution of the acoustic flux will help serve as a guide to more complete theoretical investigations.

ACKNOWLEDGMENTS

The author is very grateful to Professor Ralph Bray for helpful advice and constant encouragement throughout the course of this work. He is also indebted to P. O. Sliva, C. S. Kumar, and J. B. Ross for many valuable discussions, and to Professor R. J. Sladek for supplying some of the GaAs and Professor H. J. Yearian for orientating the samples.

APPENDIX A: ENERGY DENSITY AND RESOLUTION

The theoretical intensity of Brillouin scattering from an *equilibrium thermal distribution* of acoustic waves is essentially independent of scattering angle for $\theta' < 17^\circ$, the maximum internal angle in GaAs [see Eq. (15)]. According to the Debye theory however, the thermal-energy density (per unit bandwidth) of the acoustic waves is proportional to the square of the acoustic frequency. Thus, for thermal phonons the *angular dependence of the scattering intensity does not reflect the spectral distribution of the acoustic energy*, and therefore, an f^2 conversion must be made. This f^2 correction must also be made to scattering data on a small amplified distribution, if the distribution has been adequately resolved. By this we mean that the volume of \vec{q} space probed by the light beam falls well within the cone of the amplified phonon beam. This

is not always so, and the question of resolution and its effect on conversion from scattering intensity to phonon intensity will be considered in some detail below. In general, for a nonequilibrium distribution of acoustic waves (as we have in the acoustoelectric domain), the frequency of *maximum scattering intensity* is not to be confused with the frequency of maximum *energy density*.

Proper analysis of scattering data requires some consideration of the resolution of \vec{q} space (i. e., the frequency and propagation direction of the phonons which scatter light into the detector), as well as temporal and spatial resolution of the propagating domain. The band of phonon frequencies Δf which scatter light into the detector is determined by two factors: (a) the spectral purity of the light source $\Delta\lambda/\lambda_0$ and (b) the angular aperture of the collection optics $\Delta\theta_{\parallel}$ parallel to the plane of incidence. From Eq. (19), we find

$$\Delta f = f(\Delta\lambda/\lambda_0) + (v_s/\lambda_0)\Delta\theta_{\parallel}\cos(\frac{1}{2}\theta). \quad (\text{A1})$$

Generally, at high frequencies ($f > 3$ GHz), $\Delta\lambda$ limited our resolution, whereas at low frequencies $\Delta\theta_{\parallel}$ was the limiting factor.

The angular spread of the phonons $\Delta\delta_{\parallel}$ parallel to the plane of incidence, which scatter light into the detector, can be determined from Eq. (18), where we find

$$\Delta\delta_{\parallel} = (\Delta\theta_{\parallel}/2n_0)\cos(\frac{1}{2}\theta). \quad (\text{A2})$$

A 10° cone of flux is easily resolved in this plane, as $\Delta\delta_{\parallel}$ is less than 1° for $\Delta\theta_{\parallel}$ as large as 7° .

Perpendicular to the plane of incidence, resolution is not easily achieved. The angular spread of the phonons $\Delta\delta_{\perp}$ which scatter light into the detector can be seen from the vector diagram in Fig. 20(a), where the internal collection cone Ω' is defined by the dotted line. The maximum angle the phonon makes with the $[110]$ direction δ_{\perp} is given by

$$\tan\delta_{\perp} = k\theta'_{\perp}/q_0, \quad (\text{A3})$$

where $\theta'_{\perp} = \Delta\theta_{\perp}/2n_0$, with $\Delta\theta_{\perp}$ being the angular aperture of the collection optics (perpendicular to the plane of incidence). Consequently, the resolution in this plane is

$$\Delta\delta_{\perp} = 2 \tan^{-1}(v_s\Delta\theta_{\perp}/2\lambda_0 f_0). \quad (\text{A4})$$

As $f_0 = v_s q_0/2\pi$ is decreased below ~ 1 GHz, $\Delta\delta_{\perp}$ can become very large.

In parts (b) and (c) of Fig. 20 we show the portions of \vec{q} space (shaded areas) sampled by collection optics with $\Delta\theta_{\parallel} = \Delta\theta_{\perp} = 5^\circ$ and $\Delta\lambda/\lambda_0 = 0.1$ for the cases where the central frequencies detected

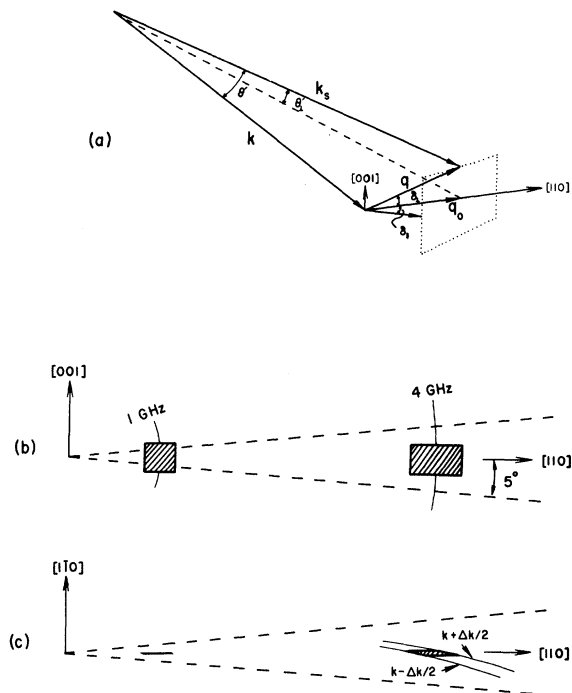


FIG. 20. (a) Vector diagram illustrating the range of phonons which scatter light into a set of collection optics defined by the dotted lines. (b) and (c) Projections in \vec{q} space. The shaded areas define the volume probed by a 5° collection aperture and 10% spread in optical wavelengths, at $\theta = 17^\circ$ and $\theta = 72^\circ$.

are 1 GHz ($\theta = 17^\circ$) and 4 GHz ($\theta = 72^\circ$), propagating along the $[110]$ axis. The dashed lines define a 10° cone of flux, which, as shown, is easily resolved in the (001) plane. Although any phonon with \vec{q} terminating between the two spheres of radii $k - \frac{1}{2}\Delta k$ and $k + \frac{1}{2}\Delta k$ satisfies the energy and momentum conditions for scattering, only those in the shaded area scatter light into the detector. In the (110) plane [Fig. 20(b)], the situation is complicated, as the light probe resolved the 10° cone at 4 GHz, but not at 1 GHz. This presents some difficulty in determining the relative energy at these two frequencies from the scattering signals. Since $\Delta\delta_{\perp} \sim f^{-1}$ in the limit of a completely unresolved angular distribution of flux, a further data correction of the form f^{-1} must be made in order to determine the energy density. Conversion from scattering intensity to energy density would then involve a factor f , rather than f^2 . Even in the partially resolved case, an appropriate correction factor can be determined if the angular distribution of the flux is known. Here, of course, proper conversion will involve a factor stronger than f , but weaker than f^2 .

APPENDIX B: INTENSE SCATTERING

The derivation of Eq. (15) was based on the assumption that the scattering produced negligible attenuation of the light beam. This is not always the case. At times the domain-induced scattering became so intense that nearly 90% of the light was scattered out the incident beam. Obviously, the depletion of the beam must be taken into account if one is to obtain a meaningful measure of the acoustic intensity.

The intensity I_t of the unscattered transmitted beam can be expressed by

$$I_t = I_0 e^{-\sigma b}, \quad (\text{B1})$$

where I_0 is the intensity of the transmitted beam in the absence of scattering, b is the optical path length, and σ is the *total scattering coefficient*. Ordinarily, $\sigma b \ll 1$ and $I_t = I_0$. When the scattering is weak, the intensity scattered into Ω' is given by

$$I_s(\Omega')/I_0 = \sigma_{\Omega'} b. \quad (\text{B2})$$

In the case of thermal scattering, the coefficient $\sigma_{\Omega'}$ is given by Eq. (15). For intense scattering ($\sigma b \sim 1$), $\sigma_{\Omega'}$ is no longer simply given by $I_s(\Omega')$. Of the two, $\sigma_{\Omega'}$ is the more fundamental quantity as it is proportional to the acoustic intensity and is independent of the length of sample traversed by the light beam.

For an equilibrium thermal distribution of phonons, σ is relatively insensitive to small changes in the direction of the incident beam. However, for a narrow cone of flux (as in the acoustoelectric domain), σ can be highly sensitive to such changes. If intense scattering occurs, $\sigma_{\Omega'}$ cannot be obtained from $I_s(\Omega')/I_0$ data without detailed knowledge of σ . However, we can obtain an expression for $\sigma_{\Omega'}$ if we simply assume that the probability of scattering is independent of the number of times the photon has been previously scattered, i. e., the deflected photons experience the same σ as the undeflected ones. This assumption is not as unrealistic as it might seem. For example, if a photon undergoes a *Stokes* scattering by a phonon in the center of the axial cone, the distribution of acoustic flux subsequently presented to this scattered photon will be a mirror image of the distribution before scattering. The scattered photon can now undergo *anti-Stokes* scattering from any of the phonons that were available to it before scattering the first time. Since the probabilities for Stokes and anti-Stokes scattering are essentially the same, the probability of scattering a second time will be equal to the initial probability. However, if the photon is scattered initially by an off-axis phonon, the probability of scattering a second time can be either *more* or *less* than the

initial probability. With this in mind, let us now proceed with the above assumption.

The net amount of light $dI_s(\Omega')$ scattered into Ω' , while propagating a distance dz into the sample is

$$dI_s(\Omega') = \sigma_{\Omega'} (I_0 e^{-\sigma z}) dz - \sigma I_s(\Omega') dz. \quad (\text{B3})$$

The first term on the right-hand side is the amount of light scattered into Ω' , where the depletion of the unscattered beam is taken into account. The second term is the amount scattered out of Ω' . Integrating over the optical path yields

$$I_s(\Omega')/I_0 = \sigma_{\Omega'} b e^{-\sigma b}. \quad (\text{B4})$$

Substituting from Eq. (B1), we find

$$\sigma_{\Omega'} b = I_s(\Omega')/I_t. \quad (\text{B5})$$

Thus, the depletion of the unscattered beam is taken into account by normalizing the scattering signal $I_s(\Omega')$ to the unscattered transmitted signal I_t .

When light is scattered by shear waves it can undergo a 90° change in polarization. However, if the photon is scattered twice its polarization will revert back to the initial polarization. Thus, the polarization of the scattered photons reveals whether or not they were scattered an odd or even number of times, but not how *many times*. This can present some problems when the acoustic flux is very intense and the probability of scattering more than once is very high.

Let us continue along the same line as above and calculate the relative intensity of the light scattered once, twice, thrice, etc. The net amount of light dI_1 scattered only once *in any direction* when the beam propagates a distance dz is given by

$$dI_1 = \sigma (I_0 e^{-\sigma z}) dz - \sigma I_1 dz. \quad (\text{B6})$$

Integrating this equation, we have

$$I_1/I_0 = \sigma b e^{-\sigma b}. \quad (\text{B7})$$

Proceeding in the same manner, we find that the fraction scattered n times is given by

$$I_n/I_0 = (1/n!) (\sigma b)^n e^{-\sigma b}. \quad (\text{B8})$$

The fraction of scattered light polarized at 90° with respect to the incident beam (I_{\perp}/I_0) is just the sum of the odd-numbered fractions given by Eq. (B8), whereas the even-numbered fractions represent the amount with polarization parallel to the incident beam (I_{\parallel}/I_0).

In Fig. 21 the calculated ratios $I_{\perp}/(I_0 - I_t)$, I_{\perp}/I_1 , and I_{\parallel}/I_1 are shown as a function of the depletion factor $(I_0 - I_t)/I_0$. When the scattering is weak, most of the scattered light is scattered only once, and very little scattered light has the parallel polariza-

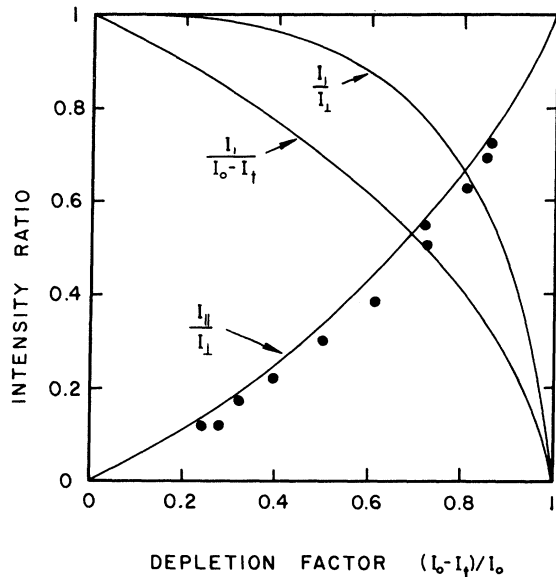


FIG. 21. $I_1/I_0 - I_t$, I_1/I_1 , and I_{\parallel}/I_{\perp} as a function of the depletion factor $(I_0 - I_t)/I_0$. Measured ratios of parallel to perpendicular intensities are shown by the data points.

tion, i. e., $I_{\parallel}/I_{\perp} \approx 0$. However, as the scattering becomes very intense, the fraction scattered only once $I_1/(I_0 - I_t)$ becomes quite small, and the ratio I_{\parallel}/I_{\perp} approaches unity. The data points represent an experimental test of this strong-scattering model.⁶⁰ With a fixed angle of incidence, the scattered light was measured at all angles on both sides of the incident beam. The data points are the ratios of the integrated intensities for the polarizations. The rather good agreement indicates that the light detected with the unchanged polarization is due to an even number of successive Brillouin scatterings.

It is important to point out that the ratio I_1/I_1 decreases rapidly when the depletion factor exceeds 50%. One must be very careful when analyzing data in this range. If a large portion of the light beam is scattered *three* times as it passes through the sample, it is not always possible to determine the acoustic frequency responsible for a particular scattering signal. For example, if phonons at the frequency of maximum scattering intensity scatter light at $\theta = 10^\circ$, then three successive scatterings from such phonons could scatter light at $\theta \approx 30^\circ$ and swamp the signal normally appearing at this angle.

[†]Work supported by the Advanced Research Projects Agency.

*Work included in a thesis in partial fulfillment of the requirements of the Ph. D. degree at Purdue University, Lafayette, Indiana.

[‡]Present address: Massachusetts Institute of Technology, Lincoln Laboratory, Lexington, Mass. 02173.

¹A. R. Hutson, J. H. McFee, and D. L. White, *Phys. Rev. Letters* **7**, 237 (1961).

²A. R. Hutson and D. L. White, *J. Appl. Phys.* **33**, 40 (1962).

³D. L. White, *J. Appl. Phys.* **33**, 2547 (1962).

⁴R. W. Smith, *Phys. Rev. Letters* **9**, 527 (1962).

⁵M. Kikuchi, *Japan J. Appl. Phys.* **2**, 807 (1963).

⁶J. H. McFee, *J. Appl. Phys.* **34**, 1548 (1963).

⁷G. Quentin and J. M. Thuillier, in *Proceedings of the International Conference on Semiconductor Physics, Paris, 1964* (Academic, New York, 1964), p. 571.

⁸W. E. Spear and P. G. LeComber, *Phys. Rev. Letters* **13**, 434 (1964).

⁹P. O. Sliva and R. Bray, *Phys. Rev. Letters* **14**, 372 (1965).

¹⁰R. Bray, C. S. Kumar, J. B. Ross, and P. O. Sliva, *J. Phys. Soc. Japan Suppl.* **21**, 487 (1966). References to many other early papers on the acoustoelectric instabilities can be found in these proceedings.

¹¹J. Zucker and S. Zemon, *Appl. Phys. Letters* **9**, 398 (1966); **10**, 212 (E) (1967).

¹²S. Zemon, J. H. Wasko, L. L. Hope, and J. Zucker, *Appl. Phys. Letters* **11**, 40 (1967).

¹³W. Wettleing, *Phys. Letters* **25A**, 193 (1967).

¹⁴J. Zucker, S. Zemon, and J. H. Wasko, in *Proceedings of the International Conference on II-VI Semiconducting Compounds, Providence, 1967*, edited by D. G.

Thomas (Benjamin, New York, 1967), p. 919.

¹⁵W. Wettleing, in *Proceedings of the International Conference on II-IV Semiconducting Compounds, Providence, 1967*, edited by D. G. Thomas (Benjamin, New York, 1967), p. 928.

¹⁶W. Wettleing and M. Bruun, *Phys. Letters* **27A**, 123 (1968).

¹⁷J. Zucker, S. Zemon, and J. H. Wasko, in *Proceedings of the Ninth International Conference on the Physics of Semiconductors*, edited by S. M. Ryvkin (Nauka Publishing House, Leningrad, 1968), p. 904.

¹⁸B. W. Hakki and R. W. Dixon, *Appl. Phys. Letters* **14**, 185 (1969).

¹⁹A. Ishida and Y. Inuishi, *J. Phys. Soc. Japan* **26**, 957 (1969).

²⁰W. Wettleing and M. Bruun, *Phys. Status Solidi* **34**, 221 (1969).

²¹S. Zemon and J. Zucker, *IBM J. Res. Develop.* **13**, 494 (1969).

²²For a discussion of these effects in CdS see, for example, J. Okada and H. Matino, *Japan. J. Appl. Phys.* **3**, 698 (1964); J. H. McFee, P. K. Tien, and H. L. Hodges, *J. Appl. Phys.* **38**, 1721 (1967).

²³The effects of inhomogeneities in GaAs have been discussed by D. L. Spears and R. Bray, *J. Appl. Phys.* **39**, 5093 (1968).

²⁴T. Bateman, H. J. McSkimin, and J. M. Whelan, *J. Appl. Phys.* **30**, 544 (1959).

²⁵D. L. Spears and R. Bray, *Appl. Phys. Letters* **12**, 118 (1968).

²⁶W. H. Hady, K. Harker, and C. F. Quate, *J. Appl. Phys.* **38**, 4295 (1967).

²⁷J. D. Maines, *Appl. Phys. Letters* **8**, 67 (1966); H. J. Fossum and A. Rannestad, *J. Appl. Phys.* **38**,

5177 (1967); A. R. Moore, *Appl. Phys. Letters* **13**, 126 (1968).

²⁸H. N. Spector, *Phys. Rev.* **127**, 1084 (1962).

²⁹C. Jacoboni and E. W. Prohofsky, *J. Appl. Phys.* **40**, 454 (1969).

³⁰M. G. Holland, *IEEE Trans. Sonics Ultrasonics* **SU-15**, 18 (1968).

³¹M. G. Holland, *Phys. Rev.* **134**, A471 (1964).

³²U. Piesbergen, *Z. Naturforsch.* **18a**, 141 (1963).

³³G. Weinreich, *Phys. Rev.* **107**, 317 (1957).

³⁴A more detailed discussion of this model is given by P. O. Sliva, Ph. D. thesis, Purdue University, 1968 (unpublished).

³⁵J. P. Rope, *Phys. Status Solidi* **21**, 517 (1967).

³⁶D. L. Spears and R. Bray, *Appl. Phys. Letters* **13**, 268 (1968); **14**, 204 (E) (1969).

³⁷G. B. Benedek and K. Fritsch, *Phys. Rev.* **149**, 647 (1966).

³⁸V. I. Nikitneko and G. P. Martynenko, *Fiz. Tverd. Tela* **7**, 622 (1965) [*Soviet Phys. Solid State* **7**, 494 (1965)]; R. W. Dixon, *J. Appl. Phys.* **38**, 5149 (1967); A. Feldman and D. Horowitz, *ibid.* **39**, 5598 (1968).

³⁹Two different filters were used in these experiments: an interference filter ($\lambda_0 = 0.99 \mu\text{m}$, $\Delta\lambda = 0.05 \mu\text{m}$) and a GaAs filter. The latter, combined with the long-wavelength cut-off of the photodiode, gave $\lambda_0 = 1.0 \mu\text{m}$ with $\Delta\lambda = 0.18 \mu\text{m}$.

⁴⁰S. Namba, *J. Opt. Soc. Am.* **51**, 76 (1961).

⁴¹T. E. Walsh, *RCA Rev.* **27**, 323 (1966); I. P. Kaminow and E. H. Turner, *Appl. Opt.* **5**, 1612 (1966).

⁴²The local drift velocity in the region of growth was used, not the average drift velocity obtained from the current. Since v_d was considerably larger than v_s and the sample was quite uniform (10%), $(v_d/v_s - 1)$ was not very sensitive to this correction.

⁴³K. R. Keller and B. Abeles, *J. Appl. Phys.* **37**, 1937 (1966).

⁴⁴E. J. Charlson and G. Mott, *Proc. IEEE* **51**, 1239 (1963); K. G. Hambleton, *Phys. Letters* **16**, 241 (1965); G. Arlt and P. Quadflieg, *Phys. Status Solidi* **25**, 323 (1968).

⁴⁵This down-shift has also been seen in CdS and ZnO. See Refs. 17-21.

⁴⁶For a discussion of current persistence see R. Bray and M. Simhony, *Phys. Letters* **29A**, 540 (1969); D. L. Spears and R. Bray, *ibid.* **29A**, 542 (1969).

⁴⁷S. Zemon, J. Zucker, J. H. Wasko, E. M. Conwell, and A. K. Ganguly, *Appl. Phys. Letters* **12**, 378 (1968).

⁴⁸It should be kept in mind that these data represent scattering intensity, not energy density. As discussed in Appendix A, a frequency-sensitive correction must

be made to convert such data into energy density. This correction decreases the intensity of the low frequencies, relative to the high frequencies, by a factor of approximately f^2 .

⁴⁹D. L. Spears and R. Bray, *Phys. Letters* **29A**, 670 (1969).

⁵⁰D. L. Spears, *IBM J. Res. Develop.* **13**, 499 (1969).

⁵¹M. Schulz and B. K. Ridley, *Phys. Letters* **29A**, 17 (1969).

⁵²D. S. Zoroglu and I. C. Chang, *Phys. Letters* **29A**, 671 (1969).

⁵³A. Many and I. Balberg, *Phys. Letters* **24A**, 705 (1967).

⁵⁴Were μE_d the correct amplification parameter, the acoustic growth rate should have increased near the end of the Ohmic regime rather than decreased as shown in Fig. 5.

⁵⁵A recent extension of small-signal theory to third order shows the v_d form of the gain expression to be valid when $E_d \gg (v_s/\mu)(2\pi f/\omega_D)^2$. See A. K. Ganguly and E. M. Conwell, *Phys. Letters* **29A**, 221 (1969).

⁵⁶This extremely simple model is capable of explaining the vast range of instabilities observed in III-V compounds, as each inhomogeneity profile will generate a different type of domain and oscillation pattern. Non-linear theory is not necessary to explain such gross features as domain formation, domain stability, and current saturation; only the more subtle features of the instability require nonlinear terms. See R. Bray, *IBM J. Res. Develop.* **13**, 487 (1969).

⁵⁷In the more strongly piezoelectric materials, such as CdS, the quantity $(v_d/v_s - 1)$ drops to such a small value (< 0.1) that it cannot be precisely determined, let alone determined whether or not it remains constant in the intense flux regime.

⁵⁸Occasionally, in some of the higher-carrier-concentration samples, the high electric field could not be maintained because of surface breakdown. Strong recombination radiation was observed in these cases, emanating from regions of visible surface damage.

⁵⁹In addition to the width of the domain increasing with applied voltage, the width has also been found to be a strong function of *circuit conditions*, i.e., whether or not constant voltage is maintained across the sample. For a fixed initial applied voltage, the steady-state domain width increased greatly with increasing series resistance, while the steady-state field remained constant. See D. L. Spears, Ph. D. thesis, Purdue University, 1969 (unpublished).

⁶⁰We are grateful to E. D. Palik for assistance with some of these measurements.

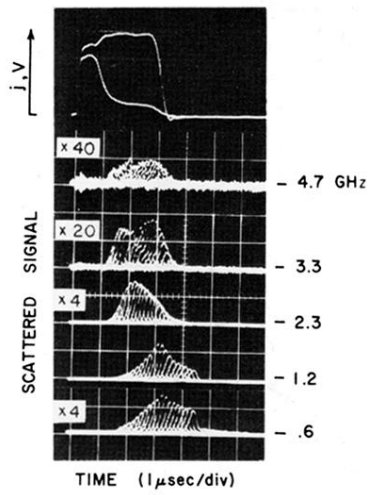


FIG. 10. Oscilloscope display of the scattering signals observed at successive positions along sample *O-2* for five different acoustic frequencies. The current and voltage traces are also shown.

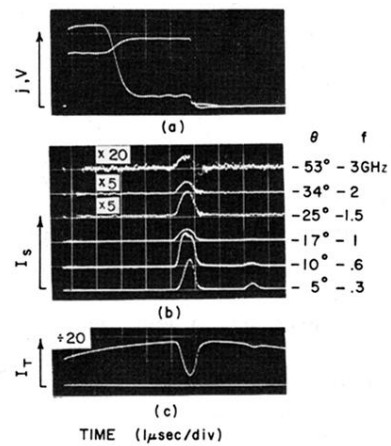


FIG. 9. Oscilloscope display of the scattering signals observed near the anode of sample R-6. The transmitted light signal $I_t(\psi = 0^\circ)$, and the current and voltage traces are also shown.